Volume 1 | Number 1 | Jan 2013 | Pages 1–100

Journal of
Materials Chemistry A

Materials for energy and sustainability
www.rsc.org/materialsA

Li⁺

e⁻

ROYAL SOCIETY
OF CHEMISTRY

The table of contents entry: A new type of Fe_3C-based ORR catalysts is reported including synthesis, tailored nanostructures, activities and active sites as well as fuel cell demonstration.

Title: Fe_3C-based Oxygen Reduction Catalysts: Synthesis, Hollow Spherical Structures and Applications in Fuel Cells

Author(s): Yang Hu, Jens Oluf Jensen, Wei Zhang, Santiago Martin, Régis Chenitz, Chao Pan, Wei Xing,* Niels J. Bjerrum and Qingfeng Li*
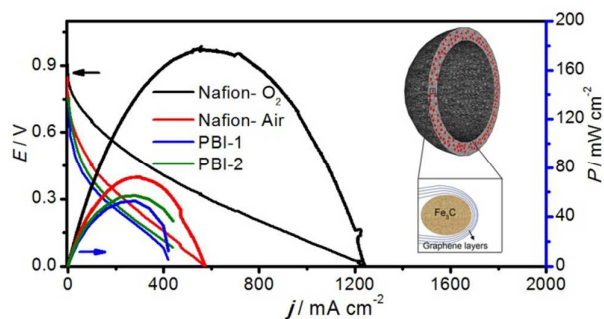
ARTICLE TYPE

Fe₃C-based Oxygen Reduction Catalysts: Synthesis, Hollow Spherical Structures and Applications in Fuel Cells

Yang Hu,[a,b] Jens Oluf Jensen,[a] Wei Zhang,[c] Santiago Martin,[a] Régis Chenitz,[d] Chao Pan,[a] Wei Xing,*[b] Niels J. Bjerrum[a] and Qingfeng Li*[a]

We present a detailed study of a novel Fe₃C-based spherical catalyst with respect to synthetic parameters, nanostructure formation, ORR active sites and fuel cell demonstration. The catalyst is synthesized by high-temperature autoclave pyrolysis using decomposing precursors. Below 500 ^{o}C, melamine-rich

10 microspheres are first developed with uniformly dispersed amorphous Fe species. During the following pyrolysis at temperatures from 600 to 660 ^{o}C, a small amount of Fe₃C phase with possible Fe-N$_x$/C active sites are formed, however, with moderate catalytic activity, likely limited by the low conductivity of the catalyst. At high pyrolytic temperatures of 700 - 800 ^{o}C, simultaneous formation of Fe₃C nanoparticles and encasing graphitic layers occur within the morphological confinement of the microspheres. With

15 negligible surface nitrogen or iron functionality, thus obtained catalysts exhibit superior ORR activity and stability. A new ORR active phase of Fe₃C nanoparticles encapsulated by thin graphitic layers is proposed. The activity and durability of the catalysts are demonstrated in both Nafion-based low temperature and acid doped polybenzimidazole-based high temperature proton exchange membrane fuel cells.

1. Introduction

Proton exchange membrane fuel cells (PEMFCs), as a clean and efficient energy conversion device, have been recognized as a possible solution for future mobile and stationary power generation applications.[1-4] One of major bottlenecks for

25 commercialization of this technology is the sluggish kinetics of the oxygen reduction reaction (ORR) at the cathode.[5] Pt-based materials have been so far the most active ORR catalysts. However, the prohibitive cost, limited availability and insufficient durability of Pt-based materials hinder the rapid and

30 widespread adoption of PEMFCs.[6] The 2013 status of platinum loading for DOE Fuel Cells Technologies Programs was 0.15 g/cm², corresponding to 0.25 g/kW(rated).[7] Using the DOE revised platinum price ($1500 per troy ounce, the average monthly price from 2006 to 2013, also the approximate current

35 price), the platinum cost counts for ca. 49% of the PEMFC stack cost or 24% of the 80 kW$_{EL}$ PEMFC system cost. As a consequence, tremendous efforts are being made to develop active and cost-effective alternative ORR electrocatalysts based on non-precious metals such as Fe and Co.[8, 9]

40 In the 1960s Jasinski discovered that cobalt phthalocyanine, a typical metal-N₄ molecule, catalyzes the ORR in alkaline media.[10] In the following decades, due to the harsh ORR conditions in acidic media, only a few types of materials have been found to be active and durable towards ORR. These include,

45 for instance, carbon-supported transition metal/nitrogen compounds (M-N$_x$/C, M = Co, Fe, Ni, etc.),[11-13] metal-free nitrogen-doped carbon materials,[14-16] transition metal chalcogenides,[17] etc. Among these candidates, the M-N$_x$/C catalysts are of most interest as they exhibit the highest ORR

50 activity and best stability close to the DOE targets.[11, 12, 18] As typically synthesized by pyrolysis of iron- and nitrogen-containing precursors, the primary active sites are believed to contain some transition metal atoms coordinated with nitrogen atoms. Three main types of sites have been identified: (i)

55 FeN₄/C sites where N is a nitrogen atom of the pyrrolic type; (ii) FeN₄/C sites where N is a nitrogen atom of the pyridinic type and (iii) CN$_x$ sites.[19] Among these three sites, the most active is the FeN₄/C of the pyridinic type for which the Fe is coordinated to the carbon support by four pairs of electrons, one pair per

60 pyridinic nitrogen atom. Concerning nitrogen precursors, it seems that the NH₃- based Fe-N$_x$/C catalyst synthesized by Lefèvre et al.[20, 21] exhibits the highest ORR activity while the polyaniline-based FeCo-N$_x$/C catalyst synthesized by Wu et al.[22, 23] shows the best durability performance in fuel cells together with a relatively

65 high activity.

Recently a novel spherical ORR catalyst was reported consisting of uniform Fe₃C nanoparticles encased by graphitic layers.[24-26] On the catalyst surface, little nitrogen or metallic functionality was detected while the catalyst exhibited high

70 activity and stability towards the ORR during rotating disk electrode (RDE) measurements. As suggested, the inner Fe₃C nanoparticles, being protected by outer graphitic layers, play a synergetic role in activating the outer graphitic layers towards the

ORR. Concerning the catalyst synthesis, only decomposing precursors (i.e. cyanamide and ferrocene) with no carbon support were used in pyrolysis. Thus the formation of unique composite nanostructures in the final catalysts would be a result of the atom-reorganization process from the vapor phase, which is interesting however with few details. Moreover, the new ORR catalyst has not been evaluated under real cathodic environments in fuel cells.

This work is devoted to a detailed study of the new Fe_3C-based oxygen reduction catalysts in terms of synthetic parameters, nanostructure formation and ORR active sites. A series of pyrolytic temperatures ranging from 500°C to 800°C were employed in the synthesis allowing for the formation of catalysts with tailored structures. Systematic characterization of the catalyst structures and correlation with their ORR performances allowed us to propose a formation mechanism of the catalysts and the existence of a new type of ORR active sites. Moreover, the activity and durability of the Fe_3C-based catalyst in fuel cells were verified in both Nafion membrane-based low temperature (LT) PEMFCs and acid-doped polybenzimidazole (PBI) membrane-based high temperature (HT) PEMFCs. To the best of our knowledge, this is the first report on the evaluation of non-precious metal ORR catalysts in HT-PEMFC.

2. Experimental

Catalyst synthesis

The composite catalysts, referred to as Fe/C-X (X stands for the pyrolytic temperature employed), was synthesized by one-step high-temperature autoclave pyrolysis. The precursors, cyanamide (99%) and ferrocene (98%) were purchased from Sigma Aldrich and used as received. A home-made 3.3-mL autoclave was assembled from stainless steel parts. A quartz cup was placed in the autoclave and in it the precursors were inserted. Typically, for the synthesis of Fe/C-X (X equals to 500, 600, 630, 660, 700 or 800), 0.467 g cyanamide and 0.052 g ferrocene were mixed and introduced into the autoclave at room temperature in a nitrogen-filled glove box. It was then closed tightly and placed at the center of a tube-furnace under a N_2 flow, which is used to protect the outside surface of the autoclave from oxidation at high temperatures. The temperature of the furnace was raised to the set value from room temperature at a rate of 10 °C min^{-1} and maintained at that temperature for 3 hours. To prevent any impurity from the autoclave inner wall, only the product inside the quartz cup was collected and used for characterizations. The obtained products (except for Fe/C-500) were acid-leached in 0.5 M H_2SO_4 at 85°C for 9 hours to remove any unstable species, followed by washing with de-ionized water and drying at 80°C under vacuum.

Physical characterizations

Nitrogen sorption isotherms were measured at 77 K with a Quadrachrome adsorption instrument. Before the analysis, the catalysts were degassed at 200 ° C for 24 h (except for Fe/C-500 which was degassed at 100 ° C). The surface area was determined using the BET method based on adsorption data in the relative pressure (P/P_0) range of 0.06 to 0.14. The bulk C and N contents in the catalysts were obtained by CHN element analysis with a Vario EL III analyzer (Germany Elementar). The bulk Fe contents in the catalysts were obtained by ICP-MS analysis with

ICAP 6000 (Thermo Fisher Scientific). X-ray diffraction (XRD) measurements were performed with a PW1700 diffractometer (Philips Co.) using a Cu Kα (λ= 1.5405 Å) radiation source. Transmission electron microscopy (TEM) images were obtained with a JEM-3000F (FEGTEM) at 300 kV. All samples for TEM analysis were the fresh products suffering no acid-leaching process, which showed a better image quality than their acid-leached counterparts. Apart from the better image quality, no obvious difference in terms of catalyst structure was observed. Scanning electron microscopy (SEM) images were taken using a LEO 1525 FE-SEM scanning electron microscope. X-ray photoelectron spectroscopy (XPS) measurements were carried out on an ESCALAB 250 (Thermo Electron) with a monochromatic Al Kα (1486.6 eV) source. Survey scans were obtained using a pass energy of 100 eV while high resolution scans of specific elements were obtained using a 20 eV pass energy. Data quantification was performed on the Avantage program. The surface atomic concentrations were determined from photoelectron peaks areas using the atomic sensitivity factors reported by Scofield. The binding energy was calibrated by placing the principal C1s peak at 284.6 eV. The fourier transform infrared spectroscopy (FT-IR) were recorded at room temperature on a Tensor 27 (Bruker) infrared spectrometer with a resolution of 4 cm^{-1}.

Electrochemical characterizations

Electrochemical measurements were conducted using Versa TAT3 Potentiostat (Princeton Applied Research) or 760C Bipotentiostat (CH Instruments). Fe/C catalyst inks were prepared by ultrasonically dispersing 10 mg of Fe/C catalyst in a suspension containing 80 μLNafion (5 wt %) solution and 514 μL ethanol, while the Pt/C catalyst (20 wt % Pt on Vulcan XC72R carbon, Johnson Matthey) ink was prepared by dispersing 5 mg catalyst ultrasonically in a mixture solution containing 50 μLNafion (5 wt %) solution, 600 μL ethanol and 400 μLMilli-Q water. The catalyst film-coated electrode was obtained by dispersing the catalyst ink on a glassy carbon rotating disk electrode (RDE) or rotating ring-disk electrode (RRDE). The catalyst loading on RRDE or RDE was 0.6 mg cm^{-2} for Fe/C catalysts and 50 μg$_{(Pt)}$ cm^{-2} for the Pt/C catalyst. A conventional three-electrode cell was employed incorporating a saturated calomel electrode (SCE) as the reference electrode, a Pt wire as the counter electrode and the RRDE or RDE as the working electrode. The reference electrode and Pt wire counter electrode were separated from the working electrode compartment using a ceramic frit and a porous glass frit, respectively. The electrolyte was 0.1 M $HClO_4$ solution. In all figures, the potentials were converted to values versus the reversible hydrogen electrode (RHE). The conversion from SCE to RHE is done by measuring the voltage ΔE between the SCE and a Pt-black coated Pt wire immersed in 0.1 M $HClO_4$ saturated with H_2. The measured ΔE was 0.305 V. RDE measurements were conducted by linear sweep voltammetry (LSV) from 1.1 V to 0.2 V at a scan rate of 10 mV s^{-1} at different rotation rates. For the RRDE test, the disc potential was scanned at 10 mV s^{-1}, while the ring electrode was held at 1.2 V vs. RHE. All the ORR currents presented in the Figures are Faradaic currents, i.e. after correction for the capacitive current. The H_2O_2 collection coefficient at the ring is determined with a $K_3Fe(CN)_6$ solution, which is 0.254

independent of rotation rates, in agreement with the value provided by the manufacturer. The following equations were used to calculate *n* (the apparent number of electrons transferred during ORR) and %H_2O_2 (the percentage of H_2O_2 released during ORR),

$$n = \frac{4I_D}{I_D + (I_R/N)} \qquad (1)$$

$$\%H_2O_2 = 100 \frac{2I_R/N}{I_D + (I_R/N)} \qquad (2)$$

where I_D is the Faradaic current at the disk, I_R the Faradaic current at the ring and N is the H_2O_2 collection coefficient at the ring. All experiments were carried out at about 25°C.

Fuel Cell tests

Single fuel cell tests with Fe/C-700 as cathode catalysts were conducted with HT-PEFMC by the DTU group and with LT-PEFMC by the INRS group.

HT-PEMFC test: The catalytic inks for cathodes were prepared with Fe/C-700 catalyst and ethanol with no ionomer. The obtained catalyst inks were then subjected to ultrasonic stirring for 1 hour. The gas diffusion layer (GDL) was a commercial carbon cloth coated with a carbon microporous layer on one side (Freudenberg H2315). The cathodes were prepared by impregnating the catalytic ink over the microporous layer of the GDL, with the catalyst loadings of 6.30 mg cm^{-2}. The anodes were commercial Pt-based electrodes with a loading of 1.56 mg$_{Pt}$cm^{-2} from Danish Power Systems. The membrane electrode assemblies (MEAs) were built by hot-pressing a H_3PO_4 doped PBI membrane (Dapozol, Danish Power Systems) with the electrodes at a temperature of 200 ℃ and a pressure of 4 MPa for 3 minutes. The HT-PEMFC tests were conducted with a commercial fuel cell hardware (Electrochem, Inc) accommodating a 5.0 cm^2 single cell geometry, which was connected to an electronic load (Hocher&Hackl ZS506). Prior to acquisition of polarization curves a conditioning process of the MEAs was carried out for 1 hour at a constant current density of 100 mA cm^{-2} and a temperature of 160°C under ambient pressure. Polarization curves were then obtained in galvanostatic mode with cell voltages being recorded after 2 minutes of running at the set current intensities. All the measurements were carried out at ambient pressure. The cell was fed with non-humidified gases (H_2/O_2). The fuel cell temperatures were 120 – 180°C. The gas flow rate was set as constant with the values corresponding to the maximum current density obtained in the polarization curve, where the stoichiometry was 1.5 for H_2 and 2 for O_2.

LT-PEFMC test: The catalyst inks were prepared using the following formulation (corresponding to an ionomer-to-catalyst ratio of 1.5): 10 mg of catalyst was mixed in a glass vial with 272 µl of Nafion 5 wt% dispersion solution, 206 µl of ethanol and 147 µl of deionized water. The inks were sonicated and agitated in a vortex mixer for a total of 1 h and then were deposited using a micropipette onto carbon paper gas diffusion layers (SGL Sigracet 25BC). The gas diffusion layer (GDL) consisted of teflonated carbon fiber paper covered with a microporous layer made of carbon black and Teflon. The electrode shape was round with area size of 1.14 cm^2 (nominal). For the catalyst ink deposition, the GDL was placed over a glass slide, which was placed over a hot plate to keep the GDL at about 100 °C during the ink deposition. The catalyst ink was deposited in several steps, each 71 microliters, corresponding to approximately catalyst of 1 mg cm^{-2} on the electrode. The catalyst loadings in the cathodes are 3.95 mg cm^{-2} for Nafion-O_2 and 4.08 mg cm^{-2} for Nafion-Air (shown in Fig. 9). The anode was prepared from a commercial Pt-based catalyst (Tanaka Kikinzoku 45.4 wt% Pt/carbon) with a loading of 0.5 mg$_{Pt}$cm^{-2}. The catalyst covered GDL, now a gas diffusion electrode (GDE), was placed in a vacuum oven to dry at 85 °C for about 1 hour. The MEA was fabricated by hot-pressing the anode and cathode on each side of a Nafion 211 membrane at 120-130℃ and a pressure of 19 MPa during 40 seconds. All MEAs were tested for 50 h or 100 h under H_2/Air or under H_2/O_2, respectively. Polarization curves were recorded by scanning the cell voltage from open circuit voltage down to 0 V at a scan rate of 0.5 mV s^{-1}. Then the fuel cell was hold at OCV again for 1 min. After that the cell voltage was held at 0.6 V or 0.4 V for a specific duration (e.g. 50 h or 100 h) and the current was recorded. Polarization curves were measured at various times throughout stability testing (Fig. S9&10). The fuel cell temperature was 80 °C; all gases were at 100% RH and at an absolute pressure of 2.0 bar on both sides. All gas flow rates were 0.3 slpm.

3.   Results and discussion

Catalyst morphology and structure
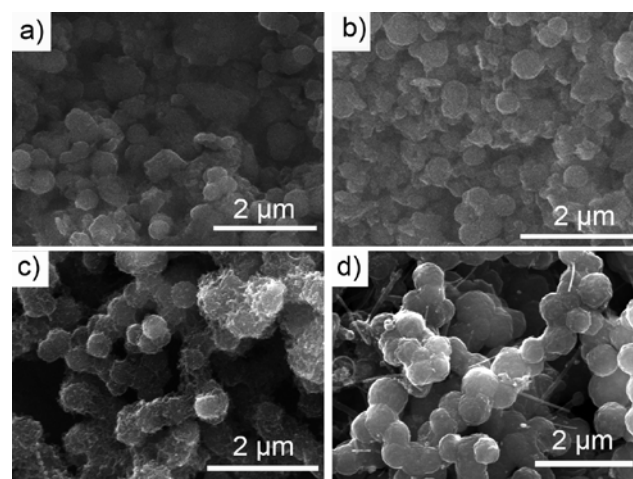
Fig. 1 SEM images of Fe/C-500 (a), Fe$_3$C/C-600 (b), Fe$_3$C/C-700 (c) and Fe$_3$C/C-800 (d).

Herein, a high temperature autoclave approach was used to synthesize the catalysts using ferrocene and cyanamide as the precursors with no carbon support. The morphologies of catalysts obtained at different pyrolytic temperatures were first investigated by SEM. As shown in Fig. 1 and Fig. S1, all the catalysts obtained with pyrolytic temperatures ranging from 500°C to 800°C primarily consisted of uniform spheres. The mean sphere diameters (estimated from analyzing SEM images) are about 410 nm for Fe/C-500 and Fe/C-600, 440 nm for Fe/C-630, Fe/C-660 and Fe/C-700, and 530 nm for Fe/C-800 (Table S1), showing an increasing trend with the pyrolytic temperature. Catalysts synthesized at high temperatures (e.g. 700°C) exhibited also more uniform morphologies of spherical structures with a few carbon nanotubes (CNTs) (Fig. S2). All the specimens for the

SEM analysis were not coated with conductive layers of carbon or gold, which means even catalysts obtained at relatively low temperatures (e.g. 500°C) from the non-conductive precursors were sufficiently electronically conductive for SEM characterization. Besides, as shown afterwards by electrochemical tests, the Fe/C-700 and Fe/C-800 catalysts exhibited much higher electronic conductivities than the Fe/C-500 and FeC-600 catalysts, which is reasonable since higher temperatures would favor the graphitization process.[27]
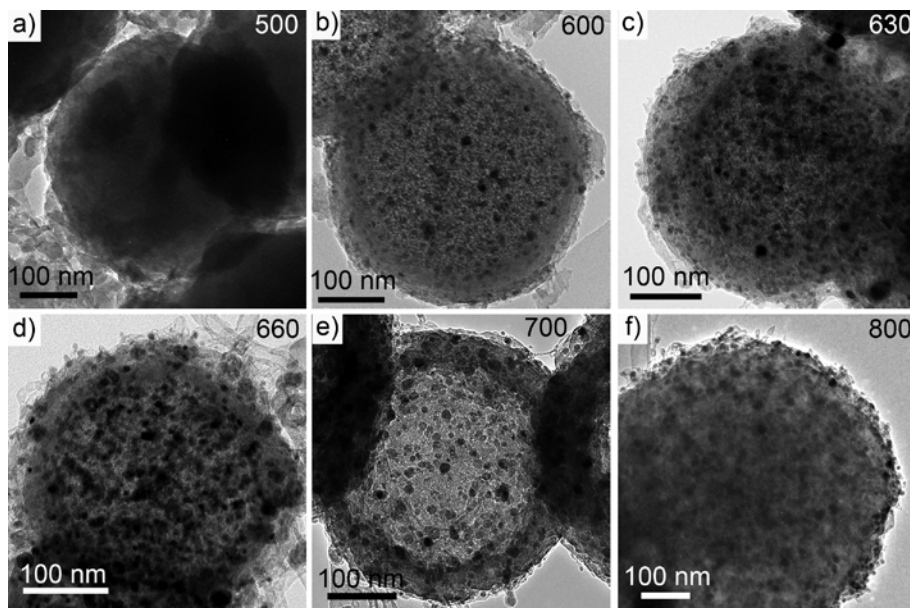
Fig. 2 TEM images of Fe/C-500 (a), Fe$_3$C/C-600 (b), Fe$_3$C/C-630 (c), Fe$_3$C/C-660 (d), Fe$_3$C/C-700 (e) and Fe$_3$C/C-800 (f) catalysts synthesized at varied pyrolytic temperatures. (Fig. 2e is reprinted from ref. 23, with kind permission from Wiley).

TEM was further used to study these catalysts, focusing mainly on the spherical structures. As shown in Fig. 2a, the spheres formed at 500°C appeared solid and uniform inside without obvious segregation phases like iron-rich particles. In comparison, the spheres obtained at 600°C (Fig. 2b) were quite different. The spheres became relatively porous inside, as indicated by the light color of the TEM image over the entire sphere area, with little variation in the outer shell zone. In addition, clearly visible iron-rich nanoparticles were dispersed within the spheres. HRTEM image (Fig. S2) shows no well-defined crystalline lattice for these particles, denoting a poor crystalline property, which is further confirmed by the XRD measurements (Fig. 5). With further increase of pyrolytic temperatures to 630 °C or 660 °C, the obtained catalyst spheres (Fig. 2c&d) showed similar porous spherical structures with the presence of more nanoparticles. It seems that the pyrolytic temperature of around 700 °C is critical. First of all the HRTEM analysis showed clear crystalline lattices characteristic of the Fe$_3$C phase in the Fe/C-700 catalyst (shown in Figure 1e of Ref. [24]). Also important was the development of the well-defined hollow spherical structure of the Fe/C-700 catalysts, as seen from the dark outer shell in Fig. 2e. This contrast distribution (from core to shell) was not changed when the sample was tilted during TEM observation. While for the Fe/C-800 catalyst, it shows only solid spheres without hollow cores, for which the reason is likely related with the higher pyrolytic temperature.

Catalyst composition and surface area
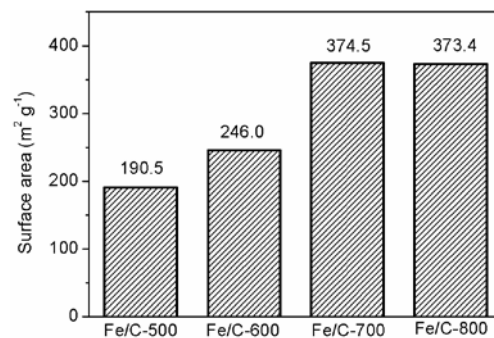
Fig. 3 Apparent BET surface areas of Fe/C-500, Fe/C-600, Fe/C-700 and Fe/C-800.
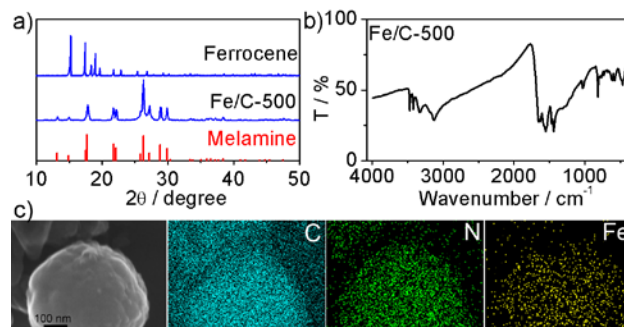
Fig. 4 (a) XRD patterns of ferrocene, Fe/C-500 and the standard XRD pattern assigned for melamine. (b) FT-IR pattern of Fe/C-500. (c) SEM image of a representative sphere of Fe/C-500 and the corresponding element mapping of C, N and Fe.
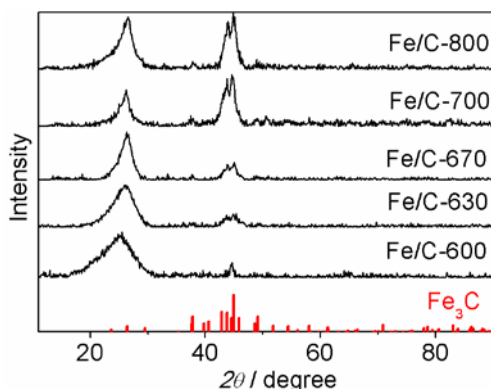
Fig.5 XRD patterns of Fe/C-600, Fe/C-630, Fe/C-660, Fe/C-700, Fe/C-800 and the standard XRD patterns assigned for Fe$_3$C.

Fig.6 Bulk C, N (wt %, determined by CHN analysis) and Fe (wt%, determined by ICP-MS) contents of catalyst synthesized at different temperatures. The surface N contents (at %) were determined by XPS analysis.

Fig. 7 High resolution XPS spectra of N-1s for Fe/C-500, Fe/C-600, Fe/C-630, Fe/C-660, Fe/C-700 and Fe/C-800, composed of mainly pyridinic N (a, 398.2 eV), pyrrolic N (b, 399.8 eV) and oxidized N (c, 401.5 eV).

Based on the morphology and structure information, BET, CHN analysis, XRD, XPS and ICP-MS would give further information on surface area and compositions of the catalysts. Fig. 3 shows apparent BET surface areas of the catalysts synthesized at various temperatures. At 500°C, the obtained catalyst shows an apparent BET surface area of 190.5 m^2 g^{-1}, relatively lower than those for catalysts synthesized at higher temperatures, e.g. 374.5 m^2 g^{-1} for Fe/C-700. The XRD pattern of Fe/C-500 showed only peaks indexed for melamine (Fig. 4a), the trimer of cyanamide, apparently from the polymerization of cyanamide under pressures. The FT-IR pattern of Fe/C-500 (Fig. 4b) is also consistent with that of melamine in literatures.[28, 29] On the other hand, as shown in Fig. 4a, ferrocene gave a standard XRD pattern of a monoclinic crystal. The disappearance of these signals in Fe/C-500 indicated the destruction of the crystalline structure of ferrocene during the pyrolysis at 500°C. Meanwhile, the elemental mapping analysis evidenced the uniform distribution of Fe, C and N through the Fe/C-500 sphere (Fig. 4c). Hence Fe species would be dispersed within the melamine-rich sphere in an amorphous form. When ferrocene alone was used as the precursor for pyrolysis at 500°C, iron carbide is formed in the product (Fig. S3), indicating the interaction between cyanamide and ferrocene in the synthesis. Besides, when ferrocene was replaced by cobaltocene or nickelocene in the synthesis, no such a spherical structure was developed at 500°C or higher temperatures (data not shown in the present work), which might be due to the higher catalytic activity of cobalt and nickel and hence the earlier carbonization[30, 31] With regard to the catalysts obtained at 600°C or higher temperatures, the corresponding XRD patterns are similar. As shown in Fig. 5, the broad peak at ca. 26.5^{o} was indexed to (002) planes of the graphitic carbon, which became sharper with the increase of pyrolytic temperatures. Aside from this peak, the rest diffraction peaks were typical of a Fe$_3$C phase (JCPDS: 65-2411)[32] (Fig.5 and Fig. S4). It is obvious that the peak intensities of the Fe$_3$C phase gradually became stronger with the increase of temperatures from Fe/C-600 to Fe/C-700 and similar for Fe/C-700 and Fe/C-800, in good agreement with the TEM results where more Fe$_3$C nanoparticles with better crystalline property were observed for catalysts obtained at higher temperatures.
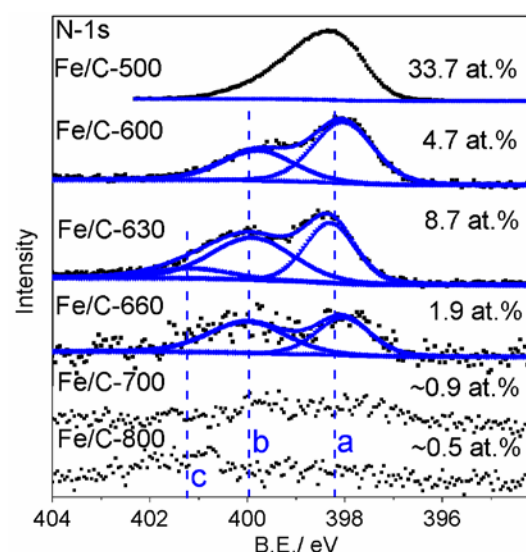
CHN analysis and ICP-MS were used to analyze the bulk C, N and Fe contents of the catalysts. As shown in Fig. 6, the bulk C contents of catalysts increase with the pyrolytic temperature while the change of bulk N contents follows a reverse trend. Consistent with the melamine-rich composition of Fe/C-500 detected by XRD, the CHN analysis reveals a high bulk content of N for Fe/C-500, i.e. 55.8 wt%. XPS was further used to analyze the near-surface N contents of these catalysts, showing a similar changing trend as that for the bulk N contents. With increasing the pyrolytic temperature from 630 ^{o}C to 800 ^{o}C, the nitrogen contents for the corresponding samples decreased gradually from 8.7 to 0.5 at.% (Fig. 7). N species for Fe/C-600, Fe/C-630, Fe/C-660 and Fe/C-700 were mainly composed of pyridinic and pyrrolic N while Fe/C-800 catalyst contained mostly oxidized N. Compared with other ORR catalysts synthesized with cyanamide as one of precursors[33-35], the N contents for the Fe/700 and Fe/800 catalysts were relatively low. On one hand, iron-rich particles might catalyze the graphitization of carbon but not nitrogen, instead they repel nitrogen from the

formed carbon structure.". On the other hand, the high-pressure environment in pyrolysis might also play a role, making the doping of N atom into carbon more difficult. Similarly, Deng *et al.* synthesized an iron-based catalyst using a high temperature autoclave approach, which contained also a negligible nitrogen content.[36] Regarding the Fe bulk content, ICP-MS measurements show a low iron content of 3.4 wt% for Fe/C-500 and higher iron contents of 6~8 wt% for Fe/C-600, Fe/C-700 and Fe/C-800. However, no obvious XPS signal of Fe-2p was observed on these catalysts (Fig. S5), indicating a complete leaching out of surface iron phases and an encapsulation structure of Fe_3C nanoparticles by carbon layers for the remaining iron species.

Speculation of the catalyst structure formation process
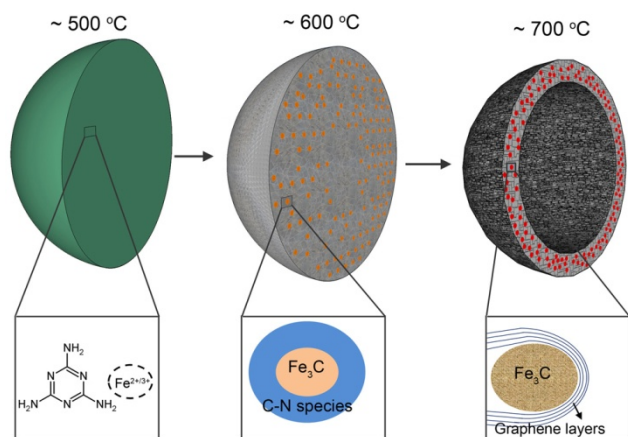
Fig. 8 Schematic representation of the structure formation mechanism for Fe/C catalysts.

Based on the results discussed above, a picture of the formation process of the spherical structure with dispersed Fe_3C nanoparticles is speculated, as shown in Fig. 8. At low pyrolytic temperatures (e.g. 500°C), cyanamide polymerizes into melamine-rich spheres in the high pressure environment. Meanwhile, ferrocene decomposes into amorphous species and disperse evenly in the sphere. With the increase of pyrolytic temperature, the melamine phase decomposes gradually into nitrogen-rich carbon (C-N) species while the amorphous iron species develops into Fe_3C nanoparticles. These Fe_3C nanoparticles then capture the formed C-N species and catalyze the formation of graphitic layers. On the other hand, the formed graphitic layers would segregate the Fe_3C nanoparticles, preventing them from further growing and therefore achieving uniform dispersion within the catalyst spheres.[37, 38]

ORR tests and active sites analysis

The ORR performance of obtained catalysts was assessed in 0.1 M $HClO_4$ by RDE and RRDE measurements. As shown in Fig. 7, alongside the change of catalyst structures with the pyrolytic temperatures, the ORR activities varied to a great extent. From Fe/C-500 to Fe/C-700, the ORR activities were monotonically increasing with the pyrolysis temperature. Further increase of the temperature to 800°C led to a slightly lower ORR activity, probably due to the smaller electrochemically accessible surface area reflected by the cyclic voltammograms (CV) tests (Fig. 9C).[39] For catalysts obtained at low temperatures, insufficient electronic conductivities due to the low graphitization degree

might be one of the reasons for their low ORR activities. The quasi-reversible $[Fe(CN)_6]^{3-/4-}$ redox was used as a probe to investigate the electronic conductivities of these catalysts. As shown in Fig. 9d, the CV curves showed standard quasi-reversible one-electron redox peaks for Fe/C-660, Fe/C-700 and Fe/C-800. The corresponding peak currents were similar to that of the bare glassy carbon electrode. For Fe/C-500, Fe/C-600 and Fe/C-630 catalysts, however, the peak currents were much smaller, indicating low conductivities of these catalysts.
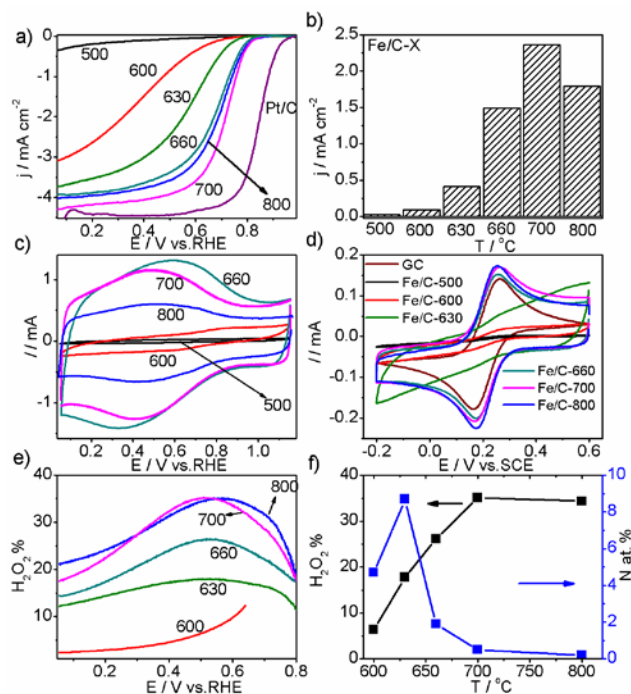
Fig. 9 (a) Linear sweep voltammograms (LSVs) of Fe/C-500, Fe/C-600, Fe/C-630, Fe/C-660, Fe/C-700, Fe/C-800 and Pt/C at 900 rpm in O_2-saturated 0.1 M $HClO_4$. The catalyst loading was 0.6 mg cm^{-2} for Fe/C catalyst and 0.25 mg cm^{-2}(50 $mg_{Pt}cm^{-2}$) for Pt/C catalyst. The scan rate was 10 mV s^{-1}. (b) ORR current densities at 0.7 V obtained from (a) for related catalysts. (c) CV curves of related catalysts at 50 mV s^{-1} in N_2 saturated 0.1 M $HClO_4$. The catalyst loadings were 117 µg for all the electrodes. (d) Cyclic voltammograms of 10 mM $Fe(CN)_6^{3-/4-}$ in 0.5 M KCl using bare RDE electrode and catalysts coated RDE electrodes. Catalyst loadings were 50 µg for all the catalysts. Scan rate is 20 mV s^{-1}. (e) Peroxide yield of related catalysts for ORR in 0.1 M $HClO_4$. Catalyst loadings were 100 µg cm^{-2} for all the electrodes. (f) Correlations of peroxide yields at 0.5 V and surface nitrogen contents of related catalysts prepared at varied pyrolytic temperatures.

Concerning the ORR pathways, RRDE measurements were made in this work to get direct monitoring of the H_2O_2 yield. As reported in literatures, for non-precious metal catalysts the loading on RRDE might have an impact on the fraction of H_2O_2 produced during the ORR.[40-42] This point was checked in the present work using Fe/C-700 as an example, showing an increase of the H_2O_2 release as the catalyst loading was decreased from 600 µg cm^{-2} to 100 µg cm^{-2} (Fig. S6). This means the oxygen reduction reaction occurs stepwise on the Fe/C-700. The released H_2O_2 molecules would be partly reduced to water at a nearby ORR site during their diffusion in the catalyst layer. Therefore, to compare the true H_2O_2 yield, the same low loading of 100 µg cm^{-2} was used for all the catalysts. The ORR current of the less active Fe/C-500 catalyst was too low to give a reliable ring current and

thus would not be discussed further. As shown in Fig. 7e, the H_2O_2 yields increased gradually from Fe/C-600 to Fe/C-700 while the Fe/C-800 yield was equal to that of Fe/C-700.

By correlating ORR activities, H_2O_2 yields with the surface N contents of these catalysts, some clues emerged as to the elucidation of active sites. First, along with the decrease of surface N contents from Fe/C-600 to Fe/C-700, ORR activities of corresponding catalysts show no decrease but an obvious enhancement, which means the well-accepted Fe-N_x center[43, 44] should not be the main active sites on the catalysts, especially for the catalysts obtained at high temperatures. Secondly, the decreasing surface N contents of catalysts from Fe/C-600 to Fe/C-800 leads an increased H_2O_2 yield for the corresponding catalysts. In particular, Fe/C-700 and Fe/C-800 show relative high H_2O_2 yields of 20-30 %, indicating a mixed (2- and 4-electron) ORR pathway. Since Fe-N_x/C active center follows a 4-electron ORR pathway,[22] this further suggests Fe/C-700 and Fe/C-800 contain a different ORR active site. Thus far, the detailed structure of the new ORR active site on Fe/C-700 and Fe/C-800 is not clear. However, as we demonstrated in our previous work, bare Fe_3C nanoparticles are acid-soluble and graphitic layers alone are not ORR active. Therefore, the synergetic interaction between Fe_3C nanoparticles and the protective graphitic layers should play key roles in the ORR.
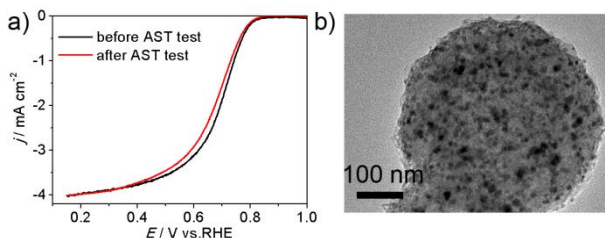
Fig. 10 (a) Polarization curves of Fe/C-800 at 900 rpm in O_2-saturated 0.1M $HClO_4$ before and after an accelerated durability test (AST). The AST was carried out with 2000 potential cycles between 0.6 and 1.0 V (8.9 hours) in O_2- saturated 0.1m $HClO_4$. (b) A representative catalyst sphere of Fe/C-800 after the AST test.

The stability of the encapsulation structure and inside Fe_3C nanoparticles was further evaluated by an accelerated stability test (AST) in the O_2 saturated $HClO_4$ solution. As shown in Fig 10, after 2000 potential cycles (8.9 hours) in O_2, the ORR activity of the Fe/C-800 remained with only a small negative shift in the half-wave potential by ca. 17 mV. After the AST test, the encapsulation structure as well as the Fe_3C nanoparticles is found to be unchanged, signifying the stability of the protected Fe_3C nanoparticles during ORR in acidic solutions.

Fuel Cell tests

The ORR performance of the best catalyst, i.e. Fe/C-700, was evaluated by single fuel cell tests. Both Nafion membrane-based LT-PEMFC and PBI membrane-based HT-PEMFC were tested. Regarding the LT-PEMFC performance, an open-circuit voltage (OCV) of 0.9 V was observed under operation with H_2/O_2 with an absolute pressure of 2.0 bar. The maximum current density reached as high as 1.2 A cm^{-2} and the peak power density was 180 mW cm^{-2} at 80 ^oC, lower than that for the state of art Pt/C cathode-based fuel cell, i.e. Nafion-Pt-O_2 in Fig. 11. When

operating with H_2/Air, the LT-PEMFC showed a reasonably lower performance with a peak powder density of 72 mW cm^{-2}. Using phosphoric acid-doped PBI membranes, the Fe/C-700 catalyst was also tested in HT-PEMFCs. Compared with the Pt/C cathode-based fuel cell (PBI-Pt in Fig. 11a), the Fe/C catalyst based HT-PEFMC exhibited a lower OCV of about 0.80 V.". The cell performance improved steadily from 120 to 180 ^oC.(Fig. S8). At 160 ^oC under ambient pressure, the maximum current density was about 445 mA cm^{-2} and the peak power density was about 60 mW cm^{-2}, respectively (Fig. 11a).
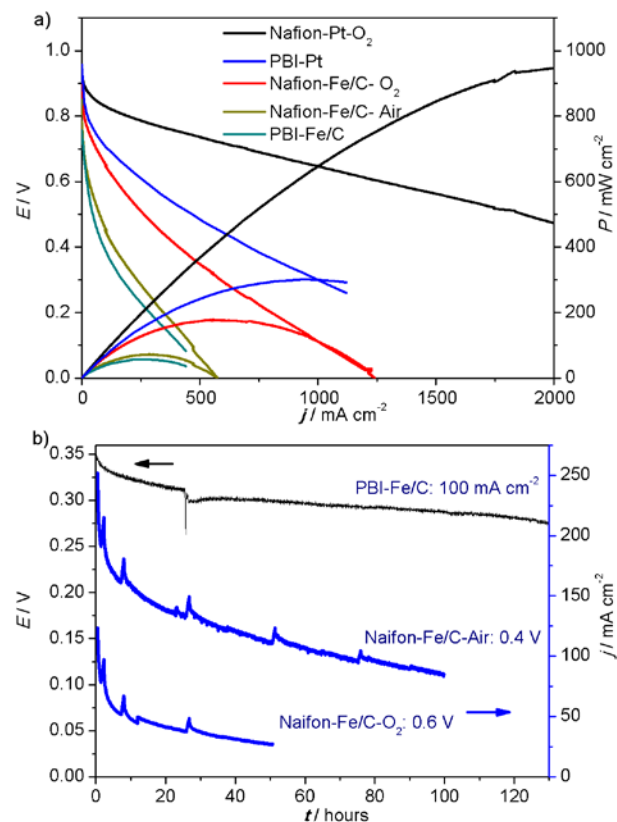
Fig. 11 (a) Polarization and power density curves for MEAs using Pt/C and Fe/C-700 in the cathodes. Nafion-O_2 or Nafion-Air indicates the tests conducted using Nafion-based LT-PEMFC fed with humidified H_2/O_2 or H_2/Air. The fuel cell temperature was 80°C. The catalyst loadings in the cathodes were 3.95 mg cm^{-2} for Nafion-Fe/C-O_2 and 4.08 mg cm^{-2} for Nafion-Fe/C-Air cells. Nafion-Pt-O_2 is the polarization curve of an MEA made with a state-of-the-art Pt-based cathode with a loading of 0.3 mg_{Pt} cm^{-2} (shown also in Figure 1a of Ref [21]). PBI-Pt and PBI-Fe/C indicate the tests conducted using acid doped PBI-based HT-PEMFC fed with non-humidified H_2/O_2. The fuel cell temperature was 160°C. The catalyst loadings in the cathodes were 1.56 mg_{Pt} cm^{-2} for PBI-Pt and 6.3 mg cm^{-2} for PBI-Fe/C cells. (b) Chronoamperometric curves at a cell voltage of 0.6 V for the Nafion-Fe/C-O_2 cell and of 0.4 V for the Nafion-Fe/C-air cell and Chrono-potentiometric curves at 100 mA cm^{-2} for PBI-Fe/C. Throughout the stability testing, polarization curves were measured at various times (shown in Fig. S9&10).

Furthermore, the durability of the catalysts in both LT- and HT-PEMFCs was studied. As depicted in Fig. 9b, a relatively fast decay on the cell current density was observed during the 50 and 100 hour test for the LT-PEMFC fed with either humidified O_2 or

air. The polarization plots obtained throughout the durability tests showed a similar trend (Fig. S9&10). The HT-PEMFC exhibited better durability during a 130 hour test (Fig. 11b). Because durability tests for LT-PEMFC and HT-PEMFC were conducted with different protocols, i.e. chronopotentiometry and chronoamperometry, respectively, we would not bring up detailed discussion in terms of fuel cell decay mechanisms in this work. More fuel cell tests with optimization of the electrode fabrication and cell operations are under the way.

4.   Conclusions

Fe_3C-based ORR catalysts in form of hollow microspheres comprising uniform Fe_3C nanoparticles encased were synthesized by high temperature autoclave pyrolysis. The pyrolytic temperatures play a critical role in formation of hollow morphologies of microspheres consisting of graphitic layer encapsulated Fe_3C nanoparticles and ORR active sites of the catalysts. Below 500^oC, melamine-rich microspheres were first formed with uniformly dispersed amorphous Fe species. At temperatures above 600^oC, the melamine-rich phase started to evaporate while the initially formed sphere structure confine the following growth of the graphitic phases as well as the encapsulated Fe_3C nanoparticles. Simultaneous formation of Fe_3C nanoparticles and electronically conductive graphitic phases occurred at 700^oC. Around this temperature the synthesized catalysts, with negligible surface nitrogen or iron functionalities, exhibit superior ORR activity and stability due to a proposed active structure, i.e. Fe_3C nanoparticles encapsulated by thin graphitic layers. Fuel cell evaluation of the catalysts is conducted using both Nafion- and PBI-based membranes in an operating temperature range from 80 to 180 ^oC with demonstrated activity and durability.

Acknowledgements

Notes and references

^{a} Department of Energy Conversion and Storage, Technical University of Denmark, Kemitorvet 207, 2800 Lyngby, Denmark; E-mail: qfli@dtu.dk
^{b} Laboratory of Advanced Power Sources, Changchun Institute of Applied Chemistry, Chinese Academy of Sciences, 130022, Changchun, China; E-mail: xingwei@ciac.ac.cn
^{c} Department of Energy Conversion and Storage, Technical University of Denmark, RisØ campus, Frederiksborgvej 399, 4000, Roskilde, Denmark
^{d} Institut National de la RechercheScientifiqueEnergie, Matériaux et Télécommunications, 1650 boulevard Lionel Boulet, Varennes (Qc) J3X 1S2, Canada
† Electronic Supplementary Information (ESI) available: [SEM and TEM images, Fe-2p XPS spectra, RRDE tests of Fe/C-700 with different catalyst loadings, polarization curves of LT-PEMFC and HT-PEMFC, etc.]. See DOI: 10.1039/b000000x/

1.   B. C. H. Steele and A. Heinzel, *Nature*, 2001, **414**, 345-352.
2.   M. K. Debe, *Nature*, 2012, **486**, 43-51.
3.   H. A. Gasteiger and N. M. Markovic, *Science*, 2009, **324**, 48-49.
4.   M. Winter and R. J. Brodd, *Chem. Rev.*, 2004, **104**, 4245-4269.
5.   Y. Bing, H. Liu, L. Zhang, D. Ghosh and J. Zhang, *Chem. Soc. Rev.*, 2010, **39**, 2184-2202.
6.   R. Borup, J. Meyers, B. Pivovar, Y. S. Kim, R. Mukundan, N. Garland, D. Myers, M. Wilson, F. Garzon, D. Wood, P. Zelenay, K. More, K. Stroh, T. Zawodzinski, J. Boncella, J. E. McGrath, M. Inaba, K. Miyatake, M. Hori, K. Ota, Z. Ogumi, S. Miyata, A. Nishikata, Z. Siroma, Y. Uchimoto, K. Yasuda, K.-i. Kimijima and N. Iwashita, *Chem. Rev.*, 2007, **107**, 3904-3951.
7.   S. Jacob and M. Jason, http://energy.gov/sites/prod/files/2014/03/f11/13012_fuel_cell_syste m_cost_2013.pdf.
8.   C. W. B. Bezerra, L. Zhang, K. C. Lee, H. S. Liu, A. L. B. Marques, E. P. Marques, H. J. Wang and J. J. Zhang, *Electrochimica Acta*, 2008, **53**, 4937-4951.
9.   L. Zhang, J. J. Zhang, D. P. Wilkinson and H. J. Wang, *J. Power Sources*, 2006, **156**, 171-182.
10. R. Jasinski, *Nature*, 1964, **201**, 1212-&.
11. F. Jaouen, E. Proietti, M. Lefevre, R. Chenitz, J. P. Dodelet, G. Wu, H. T. Chung, C. M. Johnston and P. Zelenay, *Energy Environ. Sci.*, 2011, **4**, 114-130.
12. Z. Chen, D. Higgins, A. Yu, L. Zhang and J. Zhang, *Energy Environ. Sci.*, 2011, **4**, 3167-3192.
13. Y. Hu, X. Zhao, Y. Huang, Q. Li, N. J. Bjerrum, C. Liu and W. Xing, *J. Power Sources*, 2013, **225**, 129-136.
14. Y. Y. Shao, J. H. Sui, G. P. Yin and Y. Z. Gao, *Appl. Catal. B-Environ.*, 2008, **79**, 89-99.
15. Z. Lin, G. Waller, Y. Liu, M. Liu and C.-P. Wong, *Advanced Energy Materials*, 2012, **2**, 884-888.
16. S. Wang, L. Zhang, Z. Xia, A. Roy, D. W. Chang, J.-B. Baek and L. Dai, *Angew. Chem. Int. Ed.*, 2012, **51**, 4209-4212.
17. H. Wang, Y. Liang, Y. Li and H. Dai, *Angew. Chem. Int. Ed.*, 2011, **50**, 10969-10972.
18. D. S. Su and G. Sun, *Angew. Chem. Int. Ed.*, 2011, **50**, 11570-11572.
19. U. I. Kramm, M. Lefèvre, N. Larouche, D. Schmeisser and J.-P. Dodelet, *J. Am. Chem. Soc.*, 2013, **136**, 978-985.
20. M. Lefevre, E. Proietti, F. Jaouen and J.-P. Dodelet, *Science*, 2009, **324**, 71-74.
21. E. Proietti, F. Jaouen, M. Lefevre, N. Larouche, J. Tian, J. Herranz and J.-P. Dodelet, *Nature Communications*, 2011, **2**.
22. G. Wu, K. L. More, C. M. Johnston and P. Zelenay, *Science*, 2011, **332**, 443-447.
23. G. Wu, C. M. Johnston, N. H. Mack, K. Artyushkova, M. Ferrandon, M. Nelson, J. S. Lezama-Pacheco, S. D. Conradson, K. L. More, D. J. Myers and P. Zelenay, *J. Mater. Chem.*, 2011, **21**, 11392-11405.
24. Y. Hu, J. O. Jensen, W. Zhang, L. N. Cleemann, W. Xing, N. J. Bjerrum and Q. Li, *Angew. Chem. Int. Ed.*, 2014, **53**, 3675-3679.
25. J.-P. Dodelet, R. Chenitz, L. Yang and M. Lefèvre, *ChemCatChem*, 2014, n/a-n/a.
26. Y. Hu, J. O. Jensen, W. Zhang, Y. Huang, L. N. Cleemann, W. Xing, N. J. Bjerrum and Q. Li, *ChemSusChem*, 2014, n/a-n/a.
27. X. Peng, J. Chen, J. A. Misewich and S. S. Wong, *Chem. Soc. Rev.*, 2009, **38**, 1076-1098.
28. L. D. Yao, F. Y. Li, J. X. Li, C. Q. Jin and R. C. Yu, *physica status solidi (a)*, 2005, **202**, 2679-2685.
29. J. Zhang, Z. Wang, L. Li, J. Zhao, J. Zheng, H. Cui and Z. Zhu, *Journal of Materials Chemistry A*, 2014, **2**, 8179-8183.
30. O. P. Krivoruchko and V. I. Zaikovskii, *Kinet. Catal.*, 1998, **39**, 561-570.
31. K. Jiang, C. Feng, K. Liu and S. Fan, *J. Nanosci. Nanotechnol.*, 2007, **7**, 1494-1504.
32. S. Glatzel, Z. Schnepp and C. Giordano, *Angew. Chem. Int. Ed.*, 2013, **52**, 2355-2358.
33. H. T. Chung, C. M. Johnston, K. Artyushkova, M. Ferrandon, D. J. Myers and P. Zelenay, *Electrochemistry Communications*, 2010, **12**, 1792-1795.
34. D. C. Higgins, J. Wu, W. Li and Z. Chen, *Electrochimica Acta*, 2012, **59**, 8-13.
35. J. Tian, L. Birry, F. Jaouen and J. P. Dodelet, *Electrochimica Acta*, 2011, **56**, 3276-3285.

36. D. Deng, L. Yu, X. Chen, G. Wang, L. Jin, X. Pan, J. Deng, G. Sun and X. Bao, *Angewandte Chemie (International ed. in English)*, 2013, **52**, 371-375.

37. I. K. Herrmann, R. N. Grass, D. Mazunin and W. J. Stark, *Chem. Mat.*, 2009, **21**, 3275-3281.

38. X. Feng, S. W. Chee, R. Sharma, K. Liu, X. Xie, Q. Li, S. Fan and K. Jiang, *Nano Research*, 2011, **4**, 767-779.

39. G. Wu, D. Y. Li, C. S. Dai, D. L. Wang and N. Li, *Langmuir*, 2008, **24**, 3566-3575.

40. A. Bonakdarpour, M. Lefevre, R. Z. Yang, F. Jaouen, T. Dahn, J. P. Dodelet and J. R. Dahn, *Electrochemical and Solid State Letters*, 2008, **11**, B105-B108.

41. E. J. Biddinger, D. von Deak, D. Singh, H. Marsh, B. Tan, D. S. Knapke and U. S. Ozkan, *J. Electrochem. Soc.*, 2011, **158**, B402-B409.

42. F. Jaouen and J. P. Dodelet, *J. Phys. Chem. C*, 2009, **113**, 15422-15432.

43. U. I. Kramm, M. Lefevre, N. Larouche, D. Schmeisser and J.-P. Dodelet, *J. Am. Chem. Soc.*, 2014, **136**, 978-985.

44. M. Lefevre, E. Proietti, F. Jaouen and J. P. Dodelet, *Science*, 2009, **324**, 71-74.